

# Chasing the Light: Shadowing, Collimation, and the Super-Eddington Growth of Infant Black Holes in JWST-Discovered AGNs

PIERO MADAU<sup>1,2</sup>

<sup>1</sup>*Department of Astronomy & Astrophysics, University of California, 1156 High Street, Santa Cruz, CA 95064, USA*

<sup>2</sup>*Dipartimento di Fisica “G. Occhialini,” Università degli Studi di Milano-Bicocca, Piazza della Scienza 3, I-20126 Milano, Italy*

## ABSTRACT

Observations with the James Webb Space Telescope (JWST) have uncovered a substantial population of high-redshift broad-line active galactic nuclei (AGNs) characterized by moderate luminosities, weak X-ray emissions, and faint high-ionization lines, challenging conventional models of black hole growth and AGN activity. In this study, we propose that these sources are accreting at super-Eddington rates and use geometrically thick, non-advective disk models to investigate the critical roles of photon scattering, reflections, and shadowing within funnel-like structures along the disk’s rotation axis. Our models predict highly collimated radiation fields, with isotropic-equivalent luminosities vastly exceeding the Eddington limit in polar directions, and significant suppression of emission at higher inclination angles due to shadowing. These effects result in altered spectral energy distributions and pronounced anisotropies in observable properties. Key features include ultra-blue UV continuum slopes ( $\alpha = +0.5$  to  $+0.8$ ), bolometric correction factors varying by over an order of magnitude with orientation, and suppressed coronal X-ray emissions. The anisotropy and shadowing effects may also explain the observed faintness of broad high-ionization emission lines, as the viewing angle strongly modulates both continuum brightness and the illumination of the broad-line region. These findings indicate that super-Eddington accretion flows, shaped by thick disk geometries and anisotropic radiation fields, can naturally account for many puzzling features of JWST-discovered AGNs and provide new insights into black hole growth in the early universe.

## 1. INTRODUCTION

Deep surveys with the James Webb Space Telescope (JWST) have revealed an emergent population of moderate-luminosity, broad-line active galactic nuclei (AGNs) at redshifts  $z > 4$ . Their number density is approximately 100 times greater than that of UV-selected quasars at similar redshifts. These AGNs are fueled by accretion onto early massive black holes (MBHs) with masses ranging from  $10^6$  to  $10^8 M_{\odot}$  (e.g., Harikane et al. 2023; Kocevski et al. 2023; Maiolino et al. 2024a), which appear overmassive relative to the stellar masses of their host galaxies (though this interpretation is still debated; see Ananna et al. 2024). Furthermore, they display exceptionally weak X-ray emissions (e.g., Maiolino et al. 2024b; Yue et al. 2024) and faint high-ionization emission lines (Lambrides et al. 2024). These findings pose significant challenges to our understanding of MBH growth mechanisms and the true nature of high-redshift broad-line AGNs.

A leading hypothesis suggests that accretion at super-Eddington rates may provide insights into several enigmatic features of the newly discovered sources. Early supercritical accretion flows can drive the rapid growth

of light black hole seeds during brief accretion episodes (Madau et al. 2014; Volonteri et al. 2015; Pezzulli et al. 2016; Lupi et al. 2016), potentially reducing the reliance on exotic formation pathways for massive seeds during cosmic dawn. This process may also explain the presence of overmassive, “dormant” black holes near the epoch of reionization (Juodžbalis et al. 2024). In the super-Eddington thick-disk regime, the observed X-ray faintness of JWST-discovered AGNs could result from intrinsically weak coronal (hard) X-ray emission within a funnel-like reflection geometry (Madau & Haardt 2024) or obscuration at high inclination angles relative to the rotation axis (Pacucci & Narayan 2024). Under such conditions, a lower black hole mass is needed to generate the same observed luminosity, leading to reduced black hole-to-stellar mass ratios. Additionally, the anisotropic emission from super-Eddington disks could bias black hole mass estimates, producing artificially high inferred masses (King 2024) or amplifying uncertainties by up to an order of magnitude (Lupi et al. 2024). Spectral energy distribution (SED) models of advection-dominated super-Eddington “slim disks” indicate a significant lack of rest-frame UV and even optical emission (e.g., Pognan

et al. 2020), an effect that could account for the weak UV high-ionization emission lines observed in JWST broad-line AGNs (Lambrides et al. 2024). Alternative studies suggest a contrasting view, where super-Eddington accretion produces an excess of UV radiation, leading to a much bluer continuum slope in the rest-frame UV (Castelló-Mor et al. 2016; Tang et al. 2019; Netzer 2019).

Super-Eddington, non-advective flows around black holes naturally form geometrically thick,  $h/r > 1$ , accretion disks (for a review, see Abramowicz & Fragile 2013). The shape and luminosity of low-viscosity, rotating, radiation-pressure supported “tori” have been computed by several authors under a number of simplifying assumptions (e.g., Paczyński & Wiita 1980; Abramowicz et al. 1980; Sikora 1981; Wiita 1982; Wielgus et al. 2016). Such axisymmetric models differ from the advection-dominated slim disk solution with  $h/r \lesssim 0.3$  (e.g., Abramowicz et al. 1988; Sadowski 2009; Lasota et al. 2016) in that they are radiatively efficient. Numerical hydrodynamics simulations of supercritical accretion flows have shown that the vertical advection of radiation caused by magnetic buoyancy transports energy faster than radiative diffusion, allowing a significant fraction of the photons to escape from the surface of the disk before being trapped and advected into the hole (Jiang et al. 2014, 2019b). This effectively increases the height of dissipation and reduces the cooling timescale. Such flows exhibit then surprisingly large radiation efficiencies, in excess of several percent, higher than those predicted by slim disk models where advection along the radial direction rather than radiative diffusion is the dominant cooling mechanism. Simulations also reveal the formation of “puffed up”,  $h/r > 1$  accretion tori with narrow, evacuated funnels along the rotation axis (e.g., Jiang et al. 2019b; Pacucci & Narayan 2024). On the smaller scales of black hole X-ray binaries, recent X-ray polarization observations of the supercritical source Cygnus X-3 by IXPE indeed suggest the presence of a narrow funnel that collimates radiation emitted by the accretion flow and obscures the primary source from view (Veledina et al. 2024).

In this paper, we utilize the thick disk non-advective framework rather than the underluminous – for the same accretion rate – advective slim disk solution to further investigate the possibility that most JWST-discovered broad-line AGNs at high redshift may be fueled by super-Eddington accretion flows.

## 2. AN APPROACH TO SUPERCRITICAL ACCRETION

The accretion flows we are interested in are characterized by high, supercritical rates and form geometrically

and optically thick tori dominated by radiation pressure. The large thickness of the disk naturally collimates radiation along the rotation axis, producing a super-Eddington photon flux in the evacuated, centrifugally-supported funnel region. In this section (see also Madau & Haardt 2024) we provide a primer on supercritical thick disks, adopting a cylindrical coordinate system  $(r, \varphi, z)$  centered on a Schwarzschild ( $a = 0$ ) black hole of mass  $M_{\text{BH}}$ , and using a pseudo-Newtonian potential to mimic general relativistic effects:

$$\Phi = -\frac{GM_{\text{BH}}}{R - r_S}; \quad R = (r^2 + z^2)^{1/2}, \quad r_S = \frac{2GM_{\text{BH}}}{c^2}. \quad (1)$$

Here,  $R$  is the spherical radius and  $r_S$  is the gravitational (Schwarzschild) radius. The specific angular momentum  $\ell$  depends only on the position coordinate  $r$  in the case of a polytropic gas, and is assumed *a priori* to be a linear function of the form (Paczyński & Wiita 1980)

$$\ell(r) = \ell_K(r_{\text{in}}) + \mathcal{C}(r - r_{\text{in}}). \quad (2)$$

The intersections of  $\ell(r)$  with the Keplerian angular momentum distribution  $\ell_K(r) = (GM_{\text{BH}}r)^{1/2}[r/(r - r_S)]$  provides the inner edge of the torus ( $r_{\text{in}}$ ), a pressure maximum ( $r_c$ ) located in the equatorial plane within a few gravitational radii, and a transition radius ( $r_{\text{out}}$ ) where the torus solution matches to a thin accretion disk. The inner radius  $r_{\text{in}}$  lies between the marginally bound and marginally stable orbits; its location determines the efficiency of the conversion of accreted matter into radiation. Inside  $r_c$  rotation is faster than Keplerian, and the excess centrifugal force is balanced by an inwardly directed pressure gradient.

On the surface of the disk the total (gravitational plus centrifugal) effective potential vanishes, and the shape of a torus of half-thickness  $z = h(r)$  is given by

$$h(r) = \left\{ \left[ \frac{GM_{\text{BH}}(r_{\text{in}} - r_S)}{GM_{\text{BH}} - (r_{\text{in}} - r_S)J(r)} + r_S \right]^2 - r^2 \right\}^{1/2}, \quad (3)$$

where  $J(r) \equiv \int_{r_{\text{in}}}^r \ell^2(r')dr'/r'^3$  and we have neglected the thickness of the flow at the inner edge. Radiation is emitted from the photosphere at the local Eddington rate

$$\vec{F}_{\text{rad}} = -\frac{c}{\kappa_{\text{es}}} \vec{g}_{\text{eff}} = -\frac{c}{\kappa_{\text{es}}} \left( -\vec{\nabla}\Phi + \frac{\ell^2}{r^3} \hat{e}_r \right), \quad (4)$$

where  $\vec{g}_{\text{eff}}$  is the effective gravity vector perpendicular to the surface of the disk and  $\kappa_{\text{es}}$  is the electron scattering opacity. The effective temperature on the surface of the disk can be written explicitly as  $\sigma T_{\text{eff}}^4(r) = F_{\text{rad}} = (c/\kappa_{\text{es}})\sqrt{Q(r)}$ , with

$$Q(r) \equiv \frac{G^2 M_{\text{BH}}^2}{(R - r_S)^4} + \frac{\ell^4}{r^6} - \frac{2GM_{\text{BH}}\ell^2}{R(R - r_S)^2 r^2}, \quad (5)$$

where  $R(r) = [r^2 + h(r)^2]^{1/2}$  is the distance between a point on the disk's surface and the black hole. The total luminosity radiated by the torus,  $L_{\text{rad}}$ , is calculated by integrating the emitted flux over the two disk surfaces:

$$\begin{aligned} L_{\text{rad}} &= 2 \int_0^{2\pi} \int_{r_{\text{in}}}^{r_{\text{out}}} F_{\text{rad}} d\Sigma \\ &= L_{\text{Edd}} \int_{r_{\text{in}}}^{r_{\text{out}}} \frac{rR(R-r_S)^2}{G^2 M_{\text{BH}}^2 h(r)} Q(r) dr, \end{aligned} \quad (6)$$

where  $d\Sigma = [1 + (dh/dr)^2]^{1/2} r dr d\varphi$  is the area element. The total luminosity generated by viscosity in the thick portion of the disk can be written as

$$L_{\text{gen}} = \dot{M} [(e_{\text{in}} - e_{\text{out}}) - \Omega_{\text{out}}(\ell_{\text{in}} - \ell_{\text{out}})], \quad (7)$$

where  $e = |\Phi| - \ell^2/(2r^2)$  is the specific binding energy,  $\Omega = \ell/r^2$  is the angular velocity, and  $\dot{M}$  is the accretion rate. This formula is not symmetric with respect to the inner and outer edges because the torque at the inner edge vanishes, whereas it is nonzero at the outer edge. For large tori, we have  $e_{\text{out}} = 0 = \Omega_{\text{out}}\ell_{\text{out}}$ , and

$$L_{\text{gen}} = \dot{M}e_{\text{in}} = \dot{M}c^2 \frac{r_S(r_{\text{in}} - 2r_S)}{4(r_{\text{in}} - r_S)^2} \equiv \varepsilon \dot{M}c^2, \quad (8)$$

where in the second equality we have used the boundary condition  $\ell_{\text{in}} = \ell_K(r_{\text{in}})$ .

Neglecting radial advection, global energy conservation requires that the total energy gain be compensated by radiative losses,  $L_{\text{gen}} = L_{\text{rad}}$ . By equating Equations (6) and (7) one can calculate the accretion rate  $\dot{M}$ . Note that, rather than assuming a value for the constant  $\mathcal{C}$  in the specific angular momentum distribution, in these models one can equivalently specify  $\dot{M}$ .

### 2.1. Constructing Models

The inset in Figure 1 shows three representative angular momentum distributions characterizing moderately supercritical flows around black holes. We considered three values of the inner edge,  $r_{\text{in}}/r_S = 2.2, 2.3,$  and  $2.4$  (hereafter Models A, B, and C), corresponding to efficiencies of  $\varepsilon = 0.035, 0.044,$  and  $0.051$ , respectively. These are comparable to the efficiencies observed in radiation magneto-hydrodynamics simulations of moderately supercritical flows by Jiang et al. (2014,  $\simeq 4.5\%$ ), McKinney et al. (2014,  $\simeq 1\%$ ), Sadowski et al. (2015,  $\simeq 4\%$ ), Jiang et al. (2019b,  $\simeq 5\text{--}7\%$ ), and Huang et al. (2023,  $\simeq 3\%$ ), and exceeds the efficiencies predicted by slim disk models for these accretion rates (e.g., Sadowski 2009). Values for the constant  $\mathcal{C}$  in Equation (2) were chosen following Paczyński & Wiita (1980), and resulted in outer transition radii (where rotation becomes again Keplerian) of  $r_{\text{out}}/r_S = 1078, 320, 163,$  and  $103$ .

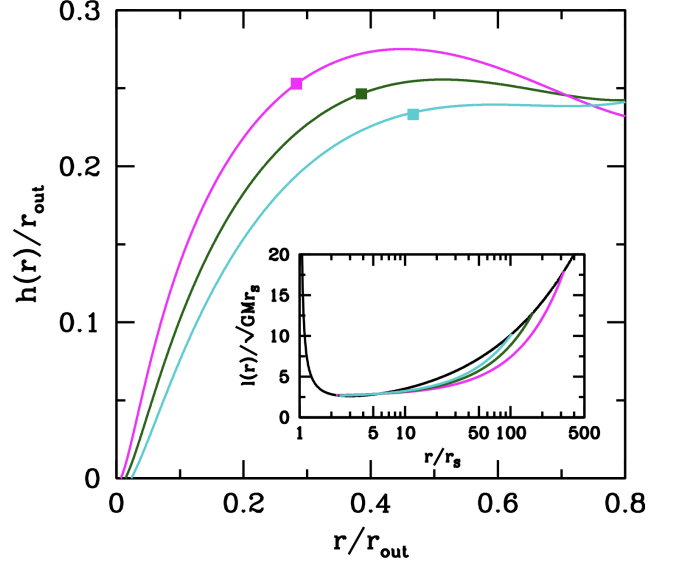


**Figure 1.** Meridional cross sections (over one quadrant) for the supercritical thick disks described by Models A (magenta curve), B (green curve), and C (cyan curve). As  $r_{\text{in}}$  decreases,  $r_{\text{out}}$  increases and so does the ratio  $L_{\text{rad}}/L_{\text{Edd}}$ , while the efficiency of mass to energy conversion becomes progressively smaller. Smaller values of  $r_{\text{in}}$  also imply steeper and deeper funnels, where pressure gradients are balanced by centrifugal forces rather than by gravity and luminosities can exceed the Eddington limit. The square symbols mark the location on the surface inside which 90% of the disk luminosity  $L_{\text{rad}}$  is actually emitted. The inset shows the Keplerian specific angular momentum distribution for the adopted pseudo-Newtonian potential (black line) and the three angular momentum distributions corresponding to our supercritical disks (Models A, B, and C).

The isotropic luminosities radiated by the thick portion of the disk ( $r < r_{\text{out}}$ ) in Models A, B, and C are  $L_{\text{rad}}/L_{\text{Edd}} = 4.3, 3.1,$  and  $2.4$ , corresponding to  $\dot{M}/\dot{M}_{\text{Edd}} = 12.5, 7.1,$  and  $4.7$ . Here we have defined the critical accretion rate  $\dot{M}_{\text{Edd}} \equiv 10 L_{\text{Edd}}/c^2$  for powering the Eddington luminosity, assuming a 10% radiative efficiency. In these models the total radiated luminosity is only logarithmically dependent on accretion rate while being linearly proportional to black hole mass,

$$L_{\text{rad}}/L_{\text{Edd}} \simeq 2.26 \ln(\dot{M}/\dot{M}_{\text{Edd}}) - 1.13. \quad (9)$$

The shapes of the thick portion of such disks (one quadrant only) are also outlined in Figure 1. The narrow, low-density funnels that develop in the innermost regions ( $dh/dr > 0, h/r > 1$ ) can be specified by the opening half-angle  $\Theta$ :

$$\Theta = \text{arccot}(h/r)_{\text{max}}. \quad (10)$$

The three configurations (Models A, B, and C) have funnel opening half-angles of  $\Theta = 35^\circ, 44^\circ,$  and  $51^\circ$ ,

**Table 1.** Properties of Thick Disks.

Parameter	Values for Models A, B, and C
$r_{\text{in}}/r_S$	2.2, 2.3, 2.4
$r_{\text{out}}/r_S$	320, 163, 103
$\epsilon$	0.035, 0.044, 0.051
$L_{\text{rad}}/L_{\text{Edd}}$	4.3, 3.1, 2.4
$\dot{M}/\dot{M}_{\text{Edd}}$	12.4, 7.1, 4.7
$\Theta$	$35^\circ$ , $44^\circ$ , $51^\circ$
$L^0/L_{\text{Edd}}$	12.3, 7.5, 5.2

respectively. The outer disk is characterized by a flattened region with  $dh/dr < 0$  and  $h/r \lesssim 1$  that eventually matches a Shakura-Sunyaev thin disk at  $r_{\text{out}}$ . As  $r_{\text{in}}$  decreases and the accretion flow becomes more super-Eddington, the disk grows larger and fatter, and more of the inner, hot and luminous, funnel regions remain hidden from view, visible only at small viewing angles from the rotation axis of the system. The 3D geometry (including shadowing) of the thick portion of a radiation-supported torus (our Model A) is shown in Figure 2 for two inclination angles.

We have added a few extra models to our main set to generate a simple best-fit ‘‘collimation angle-accretion-rate’’ relation for supercritical flows of the form:

$$\Theta = 98.5^\circ \left( \frac{\dot{M}}{\dot{M}_{\text{Edd}}} \right)^{-0.43}. \quad (11)$$

An observer looking down the rotation axis will measure a highly collimated equivalent isotropic luminosity, an angle-dependent radiation field that will be computed numerically in the next section. The main properties of our super-Eddington disk models are summarized in Table 1.

## 2.2. Anisotropic Radiation Field

Geometrical thickness causes occultation of the innermost (and hottest) disk regions for high-inclination systems, a shadowing effect that must be taken into account when discussing the observability of super-Eddington flows (e.g., Sikora 1981; Madau 1988; Wang et al. 2014; Ogawa et al. 2017). An observer at distance  $D$  from the disk will observe a bolometric flux

$$F^i = \frac{1}{D^2} \int_{\Sigma_{\text{obs}}} I(\hat{n})(\hat{n} \cdot \hat{N}) d\Sigma, \quad (12)$$

where  $\hat{N}$  is the outward normal to the surface  $z = h(r)$ ,  $\hat{n}$  is the direction of the line of sight corresponding to an inclination angle  $i$  with respect to the rotation axis ( $\hat{n} \cdot \hat{N} > 0$  for an area element to be visible to the observer), and  $\Sigma_{\text{obs}}$  is the surface area not obscured by the disk

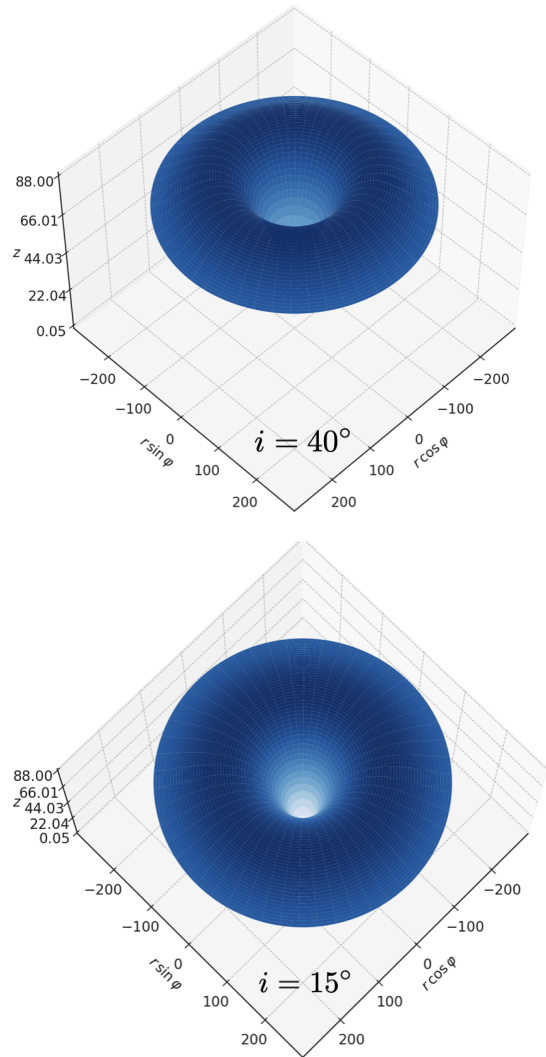


**Figure 2.** The 3D toroidal geometry (including shadowing) of the thick portion ( $r < 260$ ) of a supercritical accretion disk (Model A). The torus is observed at inclination angles  $i = 40^\circ$  (top) and  $i = 15^\circ$  (bottom), and the coordinates  $r$  and  $z$  are given in units of  $r_S$ . The shadow boundary depends on radial distance as well as azimuthal angle (see Appendix A). The unique geometry imposes pronounced anisotropy in these systems, exceeding the standard inclination-induced anisotropy of a thin accretion disk.

itself. We assume that light travels in straight lines with no Doppler and gravitational frequency shifts, and that the radiant intensity  $I(\hat{n})$  is isotropic,  $I(\hat{n}) = F_{\text{rad}}/\pi$  for  $\hat{n} \cdot \hat{N} > 0$ . And while angle-dependent relativistic effects become more pronounced the closer the emission region is to the hole, their impact on the emergent disk spectrum has been found to be typically negligible for nonspinning black holes (e.g., Zeltyn & Trakhtenbrot 2022).

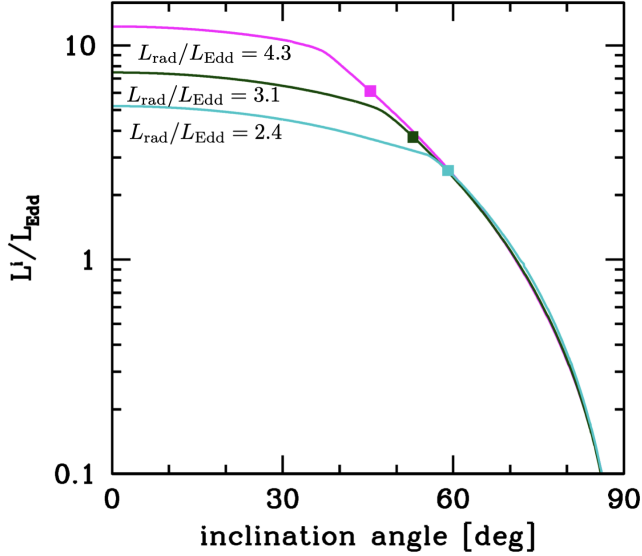


**Figure 3.** Equivalent isotropic luminosity  $L^i$  (in units of  $L_{\text{Edd}}$ ) for supercritical disk Models A (magenta line), B (green line), and C (turquoise line) as measured by an observer at different inclination angles  $i$ . The labels along the curves mark the true isotropic luminosities (in units of Eddington) radiated by the thick disks. The square symbols mark the “half-power beam width” – the inclination angle  $i_{1/2}$  at which the observed luminosity falls to 50% of the peak value. In the wider opening angle case, there is little beam-broadening by scattered radiation.

In order to get the correct angle-averaged radiation luminosity, one must also account for the fact that photons emitted within the funnel will scatter off the funnel walls many times before escaping either to infinity or falling down into the black hole. Here, we assume an optically thin funnel in which radiation is scattered off isotropically without modifying the local thermal state of the emitting material (Sikora 1981; Madau 1988). Each area element within the funnel will then see, in addition to the primary locally generated photon flux diffusing from below, incident radiation from neighboring walls that must be included in the balance of forces. In the direction normal to the surface this will be achieved if

$$F_{\text{rad}} - F_{\text{in}}^N = \frac{c}{\kappa_{\text{es}}} g_{\text{eff}}, \quad (13)$$

where  $F_{\text{in}}^N$  is the normal component of the incoming flux. Details on how to calculate viewing-angle dependent radiation fluxes including the self-illumination of the inner funnel are given in Appendices A and B. If the opening solid angle of the funnel is  $2\pi(1 - \cos\Theta)$ , then photon reflections will enhance the total surface brightness by a factor  $< (1 - \cos\Theta)^{-1}$ .

Figure 3 show the resulting “equivalent isotropic luminosity”,  $L^i \equiv 4\pi D^2 F^i$ , for different inclination angles.

Thick disks seen more edge-on,  $\Theta > 60^\circ$ , appear cooler and underluminous, never exceeding a few times  $L_{\text{Edd}}$ , independently of  $(\dot{M}/\dot{M}_{\text{Edd}})$ . At smaller inclination angles, the bottom funnel “hot spot” becomes more and more visible, and the apparent luminosity increases up to the point where the inclination angle  $i$  is approximately equal to the half-opening angle  $\Theta$ , then flattens for close to pole-on views with

$$\frac{L^0}{L_{\text{Edd}}} \simeq \left( \frac{\dot{M}}{\dot{M}_{\text{Edd}}} \right). \quad (14)$$

An observer looking along the funnel will therefore detect strongly amplified emission. Note how, even in the case of a narrow funnel, the “half-power beam width” of the thick disk – the viewing angle  $i_{1/2}$  at which the observed luminosity falls to 50% of the peak value,  $L^{i_{1/2}} = 0.5 L^0$  – is broader than the half-opening angle  $\Theta$  because radiation emitted at the bottom of the funnel is scattered sideways from the upper funnel walls into larger observer angles. In the next section we will show how the spectral energy distribution (SED) of supercritical disks exhibits an angular dependence that gets stronger with increasing photon energy.

### 2.3. Orientation-Dependent Quasi-Thermal Spectra

At the temperatures and densities of radiation-supported tori, electron scattering dominates absorption as a source of opacity, and the emitted spectrum cannot be approximated as a sum of blackbodies. For the form of the radiated specific intensity  $I_\nu(r)$ , we adopt here the modified blackbody spectrum appropriate for isotropic scattering in a constant density atmosphere (Rybicki & Lightman 1986; Czerny & Elvis 1987),

$$I_\nu = \frac{2 B_\nu(T_s)}{1 + \sqrt{1 + \kappa_{\text{es}}/\kappa_{\nu,\text{abs}}}}, \quad (15)$$

where  $B_\nu$  is the Planck function,  $T_s(r)$  denotes the characteristic disk surface temperature, and  $\kappa_{\nu,\text{abs}}$  is the sum of the free-free and bound-free absorption opacities. Assuming an empty funnel in which radiation is scattered off isotropically without modifying the local thermal state of the emitting material, the surface temperature can be derived by equating the net flux  $c g_{\text{eff}}/\kappa_{\text{es}}$  to  $\pi \int I_\nu(T_s, \rho_s) d\nu$ , where  $\rho_s$  is the characteristic disk surface density. Details of the calculations are given in Appendix C and demonstrate that supercritical tori are inefficient radiators, with lower brightness temperatures and higher color temperatures at UV and optical wavelengths compared to the blackbody temperature of a disk of the same bolometric luminosity.

Figure 4 shows our theoretical SEDs at viewing angles of  $i = 30^\circ, 60^\circ$ , and  $90^\circ$  (left panel) together

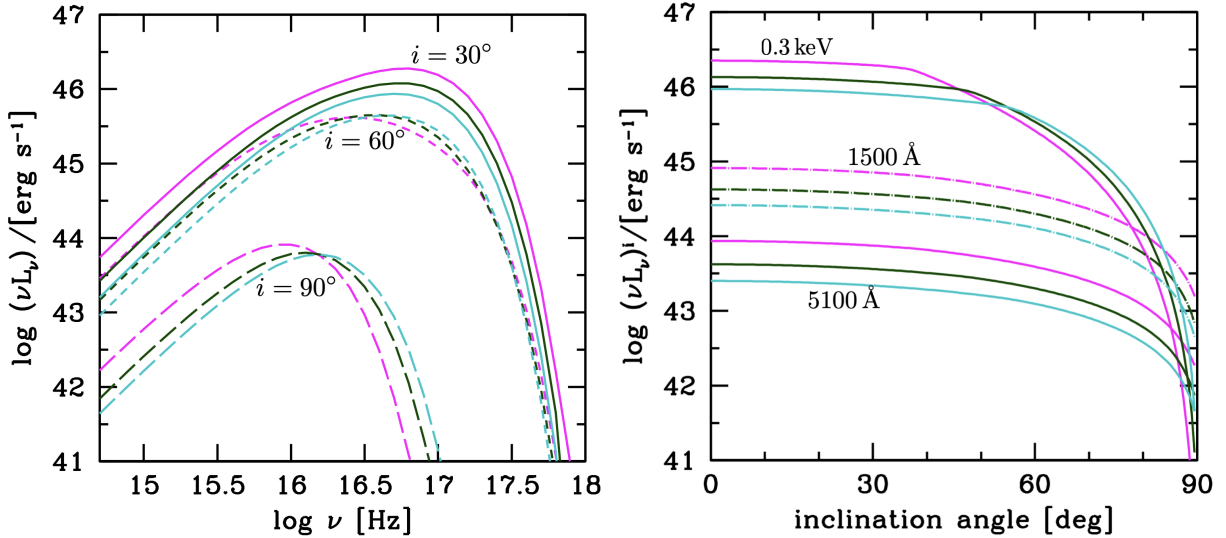


**Figure 4.** Left panel: thick disk non-blackbody spectra for Models A (magenta curves), B (green curves), and C (cyan curves), at inclination angles of  $i = 30^\circ$  (solid lines),  $i = 60^\circ$  (short-dashed lines), and  $i = 90^\circ$  (long-dashed lines). The calculations assume a black hole mass of  $M_{\text{BH}} = 10^{7.5} M_\odot$  ( $a = 0$ ), a scattering-dominated (constant density) atmosphere with gas to total pressure  $\mathcal{P} = 10^{-4}$ , and include the self-illumination effect of the funnel walls. Only the outer portions of the disk are observable when viewed edge-on, and these regions are cooler in the case of more supercritical, more extended tori. Right panel: orientation-dependent optical (5100 Å), UV (1500 Å) and soft X-ray (0.3 keV) apparent luminosities for the same models.

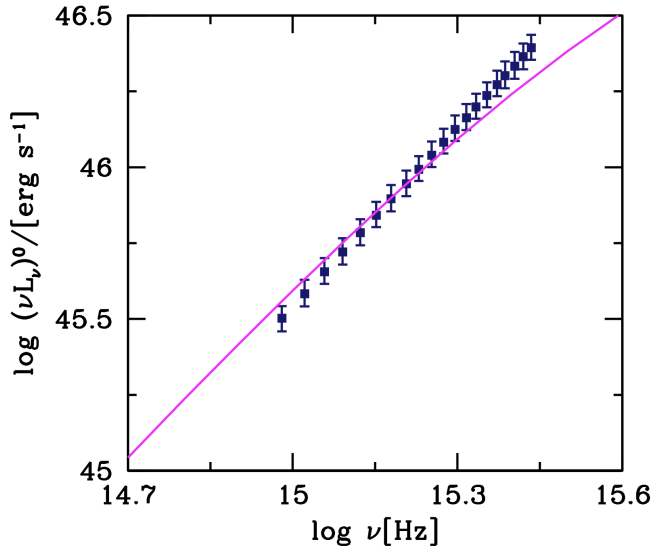


**Figure 5.** A thick disk optical-UV SED (Model A) overlaid on the rest-frame continuum spectrum of the  $z = 6.62$  quasar PSO J006+39 with  $\alpha = +0.94 \pm 0.03$  (Tang et al. 2019; Kubota & Done 2019). The solid line corresponds to inclination  $i = 0^\circ$ ,  $M_{\text{BH}} = 2.1 \times 10^8 M_\odot$  ( $a = 0$ ), and a scattering-dominated atmosphere with gas to total pressure  $\mathcal{P} = 10^{-4}$ .

with the orientation-dependent optical (5100 Å), UV (1500 Å) and soft X-ray (0.3 keV) apparent luminosities (right panel). For this calculation we have assumed a black hole mass of  $M_{\text{BH}} = 10^{7.5} M_\odot$  and a scattering-dominated (constant density) atmosphere with gas to total pressure  $\mathcal{P} = 10^{-4}$ . The frequency-dependent

anisotropy of the radiation field is evident, as the observed soft X-ray flux decreases dramatically – by nearly a factor of 30 – when the inclination increases from  $i = 30^\circ$  to  $i = 70^\circ$ . Notably, soft X-ray radiation emitted in the innermost regions, which are shadowed at high inclination angles, is scattered by the funnel walls into the line of sight even for  $i > \Theta$ . In contrast, the observed UV and optical fluxes over the same inclination range decrease less sharply, by about a factor of 3. Over the entire range  $0^\circ < i < 90^\circ$ , the drop in observed UV-optical flux is about a factor of 50 in all models.

### 3. OBSERVATIONAL IMPLICATIONS

In this section, we explore some observational implications of our findings on super-Eddington accretion flows for JWST-discovered broad-line AGNs.

#### 3.1. Weak Coronal X-ray Emission

Hard X-ray emission from AGNs is believed to result from the thermal Comptonization of optical-UV disk photons by hot electrons in an inner, tenuous corona (e.g., Haardt & Maraschi 1991). In Madau & Haardt (2024), we showed that, in the funnel-like reflection geometry that characterizes supercritical accretion, the nearly isotropic UV photon field will Compton cool coronal plasma to much lower temperatures than in the standard open geometry of a thin accretion disk, and the emitted X-ray spectrum will be extremely soft. Numerical simulations indicate that, while a thin coronal plasma with gas temperatures  $\gtrsim 10^8$  K is generated in

the inner regions of sub-Eddington accretion disks, the fraction of dissipation in this hot component decreases as the mass accretion rate increases (Jiang et al. 2019a). As simulations of mildly super-Eddington flows around non-spinning black holes also result in intrinsically weak X-ray emissions (Pacucci & Narayan 2024), we will disregard coronal Compton radiation in the following analysis.

### 3.2. Ultra-Blue UV Continuum Slopes

Our theoretical spectra exhibit a characteristic power-law form,  $L_\nu \propto \nu^\alpha$ , with  $\alpha = +0.5$  to  $+0.8$  in the UV ( $\beta = -2.5$  to  $-2.8$ , where  $L_\lambda \propto \lambda^\beta$ ). This represents an exceptionally blue SED, deviating from the standard  $\alpha = +1/3$  profile characteristic of thin accretion disks. Neither of these slope predictions align well with observations, where reddening by dust intrinsic to the source or host galaxy is commonly invoked to explain the overall redder slope observed in quasar spectra at low redshifts (Davis et al. 2007; Capellupo et al. 2015; Baron et al. 2016). There is evidence that the level of dust extinction in super-Eddington AGNs may be higher than that of slow-accreting sources (Castelló-Mor et al. 2016). Similarly ultra-blue UV spectra are measured in the hydrodynamical simulations of supercritical flows by Pacucci & Narayan (2024). Interestingly, an extremely blue slope of  $\alpha = +0.94 \pm 0.03$  has been measured in the quasar PSO J006+39, a candidate super-Eddington source at  $z = 6.62$  (Tang et al. 2019). Figure 5 compares the rest-frame optical/UV continuum spectrum of PSO J006+39 with our Model A supercritical torus, at pole-on view, for a black hole mass of  $M_{\text{BH}} = 2.1 \times 10^8 M_\odot$ . The SED of this configuration is still significantly redder,  $\alpha = +0.6$ , than PSO J006+39 (c.f. Kubota & Done 2019).

### 3.3. Bolometric Correction Factors

If comprehensive multi-wavelength photometric observations are not readily available, it becomes necessary to apply a bolometric correction to determine the AGN’s total bolometric luminosity. Our thick-disk models can provide a means of estimating characteristic bolometric correction factors for mildly supercritical flows. These factors are defined as the ratio of the total radiated luminosity to the angle-dependent equivalent luminosity emitted within a particular spectral band,

$$\kappa_{\text{band}}^i = \frac{L_{\text{rad}}}{(\nu L_\nu)_{\text{band}}^i}. \quad (16)$$

Figure 6 shows the bolometric correction factors in the optical (5100 Å) and UV (1500 Å) corresponding to the non-blackbody spectra depicted in Figure 4. These val-

ues show a clear tendency to rise sharply from pole-on to edge-on views. Additionally, they decrease at a fixed inclination angle as the accretion rate  $\dot{M}$  increases. This latter effect can be understood as being caused by the beaming/amplification of the equivalent luminosity in the denominator of the above expression. For typical viewing angles, we derive  $\kappa_{\text{UV}}^{60^\circ} = 55 - 85$  and  $\kappa_{\text{opt}}^{60^\circ} = 500 - 870$ . These values are one order of magnitude larger than the corresponding factors derived for sub-Eddington geometrically thin disks (e.g. Netzer 2019), and illustrate the big uncertainties associated with estimates of the AGN bolometric luminosity for super-Eddington sources.

### 3.4. Broad Emission Lines

The equivalent width (EW) of a hydrogen or helium recombination line in the broad-line region (BLR) of an AGN is proportional to the ratio of ionizing photons to the continuum flux beneath the line, making it a direct diagnostic tool for examining the shape of the SED. It has been predicted that supercritical sources, assuming similar BLR covering factors, would exhibit larger EWs and stronger emission lines of highly ionized species compared to sub-Eddington sources (e.g., Castelló-Mor et al. 2016; Tang et al. 2019; Ferland et al. 2020). Alternative studies have argued that photon trapping at super-Eddington rates — where the diffusion timescale for photons to escape from a thick disk surface exceeds the timescale for photons to be advected into the central black hole — results in a deficiency of UV radiation, thereby producing a significantly redder continuum slope in the rest-frame UV (Pognan et al. 2020) and weak UV high-ionization emission lines (Lambrides et al. 2024).

As demonstrated above, non-advective super-Eddington flows generate SEDs that are intrinsically very UV-bright, though their observational appearance varies significantly depending on whether they are viewed edge-on or face-on. Recent research on the structure of AGNs suggests that the clouds emitting broad lines in the UV and optical bands may be arranged in a flattened, disk-like geometry aligned with the accretion flow (e.g., Gaskell 2009; Panda 2021; Hutsemékers et al. 2023; Savić et al. 2024; Du et al. 2024). These clouds would then ‘perceive’ a different continuum SED than that observed by a typical distant observer. Below, we shall show that, in this configuration, the anisotropic radiation of a thick disk may lead to weak UV lines in type 1 AGNs, especially when observed nearly face-on.

Consider, for example, the broad line from He II (4686 Å) produced by recombinations from doubly ionized He. Due to its high ionization potential (54.4 eV),

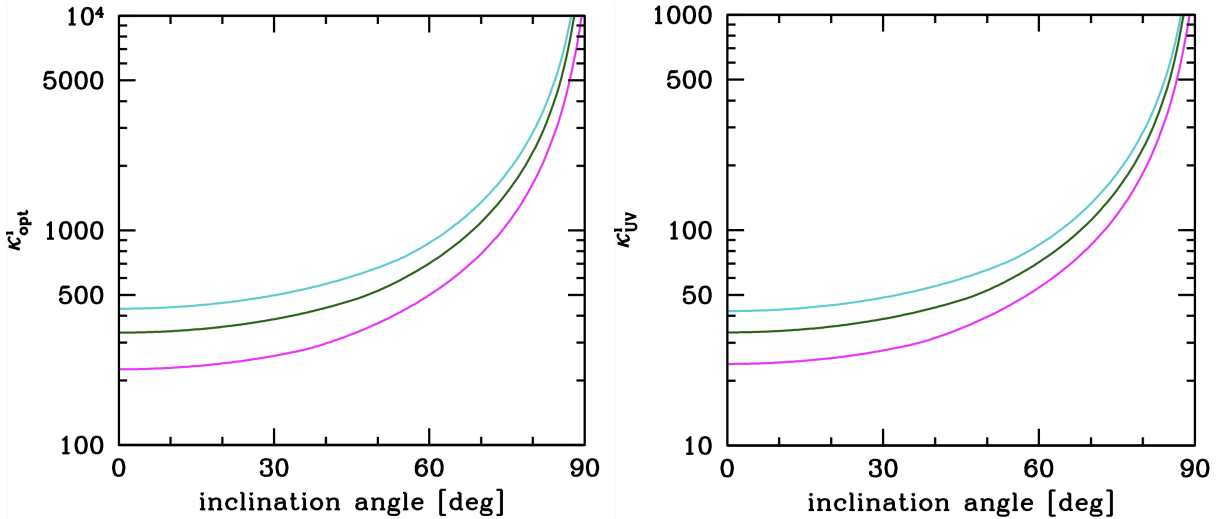


**Figure 6.** Theoretical bolometric corrections at 5100 Å (left) and 1500 Å (right) as a function of inclination angle for the super-Eddington thick disk spectra shown in Figure 4. Note the difference in  $y$ -axis scale between the two panels.

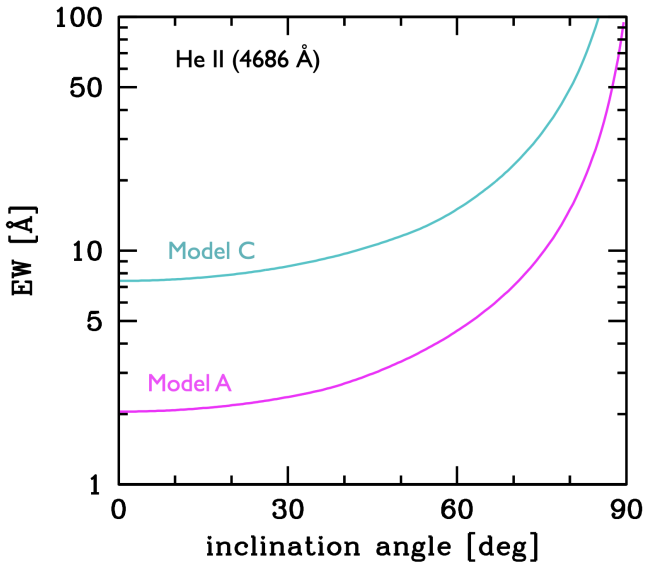


**Figure 7.** Line equivalent width (EW) of the He II emission as a function of inclination angle for Models A and C. The figure assumes a thin disk-like BLR geometry with  $i_{\text{BLR}} = 90^\circ$ , a covering factor  $(\Omega/4\pi)^{i_{\text{BLR}}} = 10\%$ , a gas temperature  $T_4 = 1$ , and a black hole mass  $M_{\text{BH}} = 10^{7.5} M_\odot$ . Observers at low inclination angles see a bright continuum that diminishes the relative strength of the He II lines, resulting in lower EWs. Conversely, at higher inclination angles, the continuum appears fainter, and the He II lines are more prominent. Notice that the line EW is smaller in more super-Eddington flows (Model A).

He II serves as a sensitive diagnostic for AGN activity, providing a clearer distinction between ionization caused by AGN and that resulting from star formation (e.g., Tozzi et al. 2023). A thick supercritical disk surrounded in its equatorial plane by BLR clouds that are

optically thick in the helium Lyman continuum would generate a number of line photons emitted per second

$$\dot{N}_{4686} = \left(\frac{\Omega}{4\pi}\right)^{i_{\text{BLR}}} Q^{i_{\text{BLR}}}(\text{He}^+) \frac{\alpha_{\text{eff}}(4686 \text{ \AA})}{\alpha_B(\text{He}^{++})}, \quad (17)$$

where  $Q^{i_{\text{BLR}}}(\text{He}^+) = \int L_\nu^{i_{\text{BLR}}} d\nu / (h\nu)$  is the number of ionizing photons above 54.4 eV emitted per second by the disk along the equatorial plane,  $(\Omega/4\pi)^{i_{\text{BLR}}}$  is the gas covering factor along the same direction – determining the fraction of radiation that is intercepted and reprocessed in the form of the HeII line emission, and the ratio  $\alpha_{\text{eff}}(4686 \text{ \AA})/\alpha_B(\text{He}^{++})$  is the fraction of helium recombinations that produce a 4686 Å photon in Case B conditions. The EW of the nebular line observed at inclination angle  $i$  would then be (Ferland et al. 2020)

$$\begin{aligned} \text{EW} &= hc \left(\frac{\Omega}{4\pi}\right)^{i_{\text{BLR}}} \frac{Q^{i_{\text{BLR}}}(\text{He}^+)}{(\nu L_\nu)_{4686}^{i_{\text{BLR}}}} \frac{\alpha_{\text{eff}}(4686 \text{ \AA})}{\alpha_B(\text{He}^{++})} \\ &\simeq 10^{-12.11} T_{4.3}^{-0.28} \left(\frac{\Omega}{4\pi}\right)^{i_{\text{BLR}}} \frac{\lambda Q^{i_{\text{BLR}}}(\text{He}^+)}{(\nu L_\nu)_{4686}^{i_{\text{BLR}}}}, \end{aligned} \quad (18)$$

where  $T_4$  is the gas temperature in units of  $10^4$  K and  $(\nu L_\nu)_{4686}^{i_{\text{BLR}}}$  is expressed in  $\text{erg s}^{-1}$ .

Let us assume, for simplicity, a thin disk-like BLR geometry in which gas clouds do not extend to high elevations above the mid-plane (e.g., Pozo Nuñez et al. 2014). Figure 7 shows the line EW for  $i_{\text{BLR}} = 90^\circ$ , a covering factor  $(\Omega/4\pi)^{i_{\text{BLR}}} = 10\%$ , a gas temperature  $T_4 = 1$ , and a black hole mass  $M_{\text{BH}} = 10^{7.5} M_\odot$ . The figure illustrates the differences in line emission properties as observed at different inclination angles for Models A and C. Observers at low inclination angles (closer to the rotation axis) see a very bright blue continuum but

weak He II lines, as the strong continuum emission outshines the line emission. Conversely, observers at higher inclination angles (closer to edge-on) see a fainter UV-optical continuum – similar to the one incident on BLR gas – and measure stronger He II lines in the spectrum.

Taking inspiration from previous studies (e.g., Wang et al. 2014), we propose that, due to geometric effects and the anisotropy of the radiation field of supercritical disks, the BLR will receive a reduced number of helium-ionizing photons. Additionally, when viewed more face-on, the brighter optical continuum beneath the line will overshadow the contribution from the BLR gas clouds. This effect may account for the weak UV lines observed in JWST-discovered broad-line AGNs at high redshift, under the assumption that these AGNs are powered by super-Eddington accretion flows. This in turn suggests smaller radial sizes for the BLR than predicted by standard photoionization modeling, and may offer an explanation for reverberation mapping- and interferometric-based claims (e.g., Du et al. 2016; GRAVITY Collaboration et al. 2024) that high Eddington ratio AGNs show consistently smaller BLR sizes than those predicted by the canonical radius-luminosity relation of

sub-Eddington AGNs. While a detailed analysis of these phenomena is beyond the scope of this study, as line EWs may be influenced by systematic uncertainties such as dust reddening, gas geometry, and cloud covering factors, we finally observe here that the strongest JWST detection of a broad He II (4686 Å) line in the galaxy GS.3073 at  $z = 5.55$  (EW  $\simeq 20$  Å; Übler et al. 2023) appears to be associated with a type 1.8 AGN. These objects are thought to be viewed at inclinations  $> 60^\circ$  (e.g., Marin 2014, and references therein), in qualitative agreement with Figure 7.

#### ACKNOWLEDGEMENTS

Support for this work was provided by NASA through grant TCAN 80NSSC21K027, by grant NSF PHY-2309135 to the Kavli Institute for Theoretical Physics (KITP), and by the Italian Ministry for Research and University (MUR) under Grant “Progetto Dipartimenti di Eccellenza 2023-2027” (BiCoQ). We acknowledge many useful discussions on this project with R. Maiolino, and are grateful to V. Bromm, B. Robertson, R. Schneider, and R. Somerville for organizing the KITP workshop “Cosmic Origins: The First Billion Years,” which provided the initial motivation for this work.

## APPENDIX

### A. SHADOWING

The radiation flux observed at distance  $D$  from the disk is

$$F^i = \frac{1}{D^2} \int_{\Sigma_{\text{obs}}} I(\hat{n})(\hat{n} \cdot \hat{N}) d\Sigma, \quad (\text{A1})$$

where  $\hat{N}$  is the outward normal to the surface,  $\hat{n}$  is the direction of the line of sight, and  $\Sigma_{\text{obs}}$  is the surface area not obscured by the disk itself. Let us specify a line of sight in the  $xz$ -plane of a Cartesian coordinate system  $xyz$  centered on the black hole, and denote with  $i$  the angle between the line of sight and the rotation  $z$ -axis. The direction vector  $\hat{n}$  can then be written as

$$\hat{n} = (\sin i, 0, \cos i). \quad (\text{A2})$$

The unit normal vector at a generic point  $P = (r \cos \varphi, r \sin \varphi, h)$  on the surface  $z = h(r)$  of the disk is

$$\hat{N} = (-\cos \varphi dh/dr, -\sin \varphi dh/dr, +1) / \sqrt{1 + (dh/dr)^2}, \quad (\text{A3})$$

and the dot product of  $\hat{n}$  and  $\hat{N}$  must be positive for the point to be visible to the observer. This *local visibility* condition yields

$$\frac{dh}{dr} \leq \frac{\cot i}{\cos \varphi}. \quad (\text{A4})$$

When this inequality is not satisfied, the surface is oriented away from the observer’s line of sight and is not visible. As  $\varphi$  approaches  $90^\circ$  and  $270^\circ$ ,  $\cos \varphi$  decreases, and more of the funnel’s surface becomes invisible to the observer. If  $i = 90^\circ$ , the observer will only see the parts of the surface that are tilting downward, i.e. where  $dh/dr < 0$ .

Even if the dot product condition above is satisfied and the point is visible by orientation, it can still be in shadow if obstructed by another part of the surface. To find the condition for shadowing, which depends on geometry of the

funnel along the line of sight, let us consider without loss of generality the element of funnel area at point  $P_0 = (r_0, 0, h_0)$  in the  $xz$ -plane, whose outward unit normal  $\hat{N}_0$  is perpendicular to the line of sight,

$$\hat{N}_0 = (-\cos i, 0, \sin i). \quad (\text{A5})$$

At  $P_0$ , the line of sight is tangent to the surface. Let us denote with  $\vec{L}$  the displacement vector connecting  $P_0$  to a generic point  $P$  on the surface of the funnel:

$$\vec{L} = (r \cos \varphi - r_0, r \sin \varphi, h - h_0). \quad (\text{A6})$$

The dot product between  $\hat{N}_0$  and  $\vec{L}$  determines the transition between visible and shadowed regions. When  $\hat{N}_0 \cdot \vec{L} > 0$ , the point  $P$  lies above the inclined line-of-sight plane and is visible to the observer, while when  $\hat{N}_0 \cdot \vec{L} \leq 0$   $P$  lies below this plane and will be shadowed by the surface at  $P_0$ . The condition  $\hat{N}_0 \cdot \vec{L} > 0$  gives

$$h - h_0 > (r \cos \varphi - r_0) \cot i. \quad (\text{A7})$$

The shadow boundary depends on both the radial distance and the azimuthal angle. The shadow forms a sector-like pattern, where points near the line of sight are more likely to be in shadow, while points farther away (near  $\varphi = 90^\circ$  or  $\varphi = 180^\circ$ ) are more likely to remain visible (see Figure 2).

## B. SELF-ILLUMINATION EFFECT

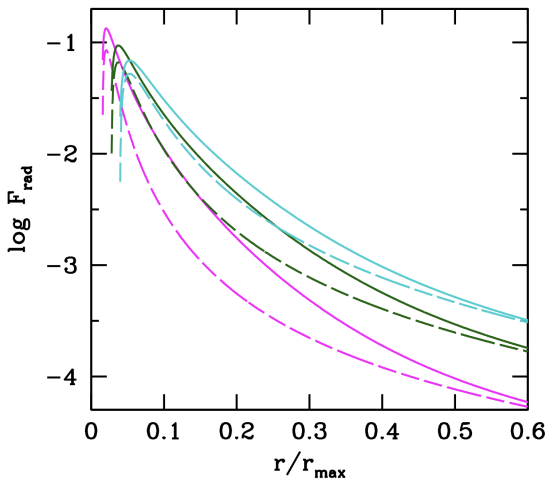


**Figure 8.** Bolometric flux emitted by the funnel walls in our thick disk models (same color coding as in previous figures). The dashed curves show the effective gravity or net flux vs. radius in the funnel (in units of the radius  $r_{\max}$  where the torus reaches its maximum height.) This is brightest near the inner edge of the disk, falling off approximately as  $r^{-2}$ . The solid curves show the flux enhancement resulting from the self-illumination of the funnel walls. If the opening solid angle of the funnel is  $2\pi(1 - \cos \Theta)$ , then photon reflections will enhance the total surface brightness by a factor  $< (1 - \cos \Theta)^{-1}$ .

number of concentric  $r$ -rings of equal radial width  $\Delta r$  and quasi-uniform emission properties, and by approximating Equation (B8) as

$$F_{\text{rad},i} - \frac{1}{\pi} \sum_j B_{ij} F_{\text{rad},j} = \frac{c}{\kappa_{\text{es}}} g_{\text{eff},i}, \quad (\text{B10})$$

where

$$B_{ij} = \frac{\hat{N}_i \cdot \vec{L}}{|\vec{L}|} \left[ \frac{(\hat{N}_j \cdot \vec{L})}{|\vec{L}|^3} d\Sigma_j \right] \quad (\text{B11})$$

Photons emitted within the funnel will in general scatter many times before escaping either to infinity or falling down into the hole. Every area element within the funnel will see incoming radiation that must be included in the balance of forces (Sikora 1981; Madau 1988) in order to get the correct angle-averaged radiation luminosity. Here, we shall assume an empty funnel in which radiation is scattered off isotropically without modifying the local thermal state of the emitting material. The balance of forces normal to the surface is now given by the implicit integral equation:

$$F_{\text{rad}} - F_{\text{in}}^N = \frac{c}{\kappa_{\text{es}}} g_{\text{eff}}, \quad (\text{B8})$$

where  $F_{\text{rad}}$  is the sum of the flux locally generated and the normal component of the incoming flux that is scattered isotropically,

$$F_{\text{in}}^N = \frac{1}{\pi} \int F_{\text{rad}} \frac{(\hat{N} \cdot \vec{L})}{|\vec{L}|} d\Omega. \quad (\text{B9})$$

Here  $d\Omega$  is the element of solid angle associated with the direction  $\vec{L}$  within which the incoming radiation is seen at a given point. The distribution of total fluxes  $F_{\text{rad}}$  can be calculated by subdividing the surface of the funnel into a finite

is the fraction of radiation emitted from the  $j$ th ring that reaches the  $i$ th ring in the solid angle given by the term in square brackets, and

$$d\Sigma_j = r_j [1 + (dh/dr)_j^2]^{1/2} d\varphi \Delta r \quad (\text{B12})$$

is the element of area. We have used a grid of 1000 points and solved the system of linear equations (B10) using LU decomposition. A substantial increase of surface brightness is observed in narrow funnels, as depicted in Figure 8. To compute how multiple scatterings modify the disk SED, Equation (B10) has to be solved at each frequency, with the local specific intensity being given by Equation (15).

It is important to stress that, while thick disk models are constructed to have normal forces at the surface in balance (see Equation B8), the tangential components of the absorbed radiation flux are left unbalanced. This will have little effect on the equilibrium structure at large optical depths, but strict hydrostatic equilibrium will not be maintained in the surface layers, and upward acceleration of the funnel walls will occur (Sikora & Wilson 1981; Narayan et al. 1983). The accretion flows discussed here, however, are only mildly super-Eddington, with  $\dot{M}/\dot{M}_{\text{Edd}}$  in the range  $\sim 5$ –12. In this regime, numerical simulations of accretion flows around nonspinning MBHs show that funnels remain optically thin and the kinetic luminosity of the outflowing material is only a few percent of the radiation luminosity (Jiang et al. 2014, 2019b).

### C. MODIFIED BLACKBODY SPECTRUM

The SEDs of our supercritical tori follow the modified blackbody spectrum appropriate for isotropic scattering in a constant density atmosphere (Rybicki & Lightman 1986; Czerny & Elvis 1987),

$$I_\nu = \frac{2 B_\nu(T_s)}{1 + \sqrt{1 + \kappa_{\text{es}}/\kappa_{\nu,\text{abs}}}}, \quad (\text{C13})$$

where  $B_\nu$  is the Planck function,  $T_s(r)$  denotes the characteristic disk surface temperature, and  $\kappa_{\nu,\text{abs}}$  is the sum of the free-free and bound-free absorption opacities. We approximate them as having the same frequency dependence, and write (see Hall et al. 2018)

$$\kappa_{\nu,\text{abs}} = \kappa_* \rho_s T_s^{-7/2} x^{-3} (1 - e^{-x}), \quad (\text{C14})$$

with  $x = h\nu/kT_s$  and

$$\begin{aligned} \kappa_* = & (3.68 \times 10^{22} \text{ cm}^5 \text{ g}^{-2} \text{ K}^{7/2}) \\ & \times [X + Y + 1180Zf(T)](1 + X), \end{aligned} \quad (\text{C15})$$

where  $X$ ,  $Y$ , and  $Z$  are the H, He, and metal mass fractions (Meier 2012), and  $f(T)$  is the fraction of metals that are not ionized (Meier 2012). At the redshifts of interest here, with early AGNs being hosted in a low metallicity environment (e.g., Maiolino et al. 2024a), we take  $X = 0.75$ ,  $Y = 0.248$ , and  $Z = 0.002$ . We also adopt  $f(T) = 0.5$ , which gives  $\kappa_* = 1.4 \times 10^{23} \text{ cm}^5 \text{ g}^{-2} \text{ K}^{7/2}$  with the above mass fractions. The electron scattering opacity is  $\kappa_{\text{es}} = 0.2(1+X) \text{ cm}^2 \text{ g}^{-1}$ .

Assume now that, throughout the disk surface layer, the ratio of gas pressure to total pressure,  $\mathcal{P}$ , is constant. This implies

$$\rho_s = \left( \frac{a_B \mu m_{\text{H}}}{3k} \right) \left( \frac{\mathcal{P}}{1 - \mathcal{P}} \right) T_s^3, \quad (\text{C16})$$

where  $a_B$  is the radiation density constant,  $k$  is the Boltzmann constant,  $m_{\text{H}}$  is the mass of the hydrogen atom, and  $\mu$  is the mean molecular weight,  $\mu = 0.59$  for low-metallicity gas that is completely ionized in H and He. In three-dimensional radiation magnetohydrodynamical simulations of supercritical disks with accretion rates comparable to our study, the inner regions of all disks have radiation pressure  $10^4 - 10^6$  times the gas pressure (Jiang et al. 2019b). Then  $\kappa_{\nu,\text{abs}} \ll \kappa_{\text{es}}$  at all relevant frequencies, and in this limit we can write

$$I_\nu = \mathcal{I}_\nu T_s^{11/4} \left( \frac{\mathcal{P}}{1 - \mathcal{P}} \right)^{1/2} \frac{x^{3/2}}{e^x (1 - e^{-x})^{1/2}}, \quad (\text{C17})$$

where  $\mathcal{I}_\nu \equiv 4(c^2 h^2)^{-1} \sqrt{(k^5 \kappa_* / 3 \kappa_{\text{es}}) a_B \mu m_{\text{H}}} = 7.2 \times 10^{-16} \text{ erg s}^{-1} \text{ cm}^{-2} \text{ Hz}^{-1} \text{ sr}^{-1} \text{ K}^{-11/4}$ . The total modified blackbody flux is

$$\pi I = \mathcal{F} T_s^{15/4} \left( \frac{\mathcal{P}}{1 - \mathcal{P}} \right)^{1/2}, \quad (\text{C18})$$

where  $\mathcal{F} \equiv 1.51 \pi \mathcal{I}_\nu k/h = 7.1 \times 10^{-5} \text{ erg s}^{-1} \text{ cm}^{-2} \text{ K}^{-15/4}$ . The surface temperature  $T_s$  obtained by equating Equation (C18) with Equation (4) is much higher in the inner regions than the effective temperature  $T_{\text{eff}}$ , and the emitted spectrum extends to higher frequencies than a simple sum-of-blackbodies. We note here the very weak dependence of the temperature  $T_s$  on the parameter  $\mathcal{P}$ ,  $T_s \propto \mathcal{P}^{-2/15}$ . Any change of  $\mathcal{P}$  will affect the disk density profile and the location of the photosphere, keeping the surface temperature  $T_s$  almost constant, independently of  $\mathcal{P}$ .

## REFERENCES

- Abramowicz, M. A., Calvani, M., & Nobili, L. 1980, *ApJ*, 242, 772
- Abramowicz, M. A., Czerny, B., Lasota, J. P., & Szuszkiewicz, E. 1988, *ApJ*, 332, 646
- Abramowicz, M. A., & Fragile, P. C. 2013, *Living Reviews in Relativity*, 16, 1
- Ananna, T. T., Bogdán, Á., Kovács, O. E., Natarajan, P., & Hickox, R. C. 2024, *ApJL*, 969, L18
- Baron, D., Stern, J., Poznanski, D., & Netzer, H. 2016, *ApJ*, 832, 8
- Capellupo, D. M., Netzer, H., Lira, P., Trakhtenbrot, B., & Mejía-Restrepo, J. 2015, *MNRAS*, 446, 3427
- Castelló-Mor, N., Netzer, H., & Kaspi, S. 2016, *MNRAS*, 458, 1839
- Czerny, B., & Elvis, M. 1987, *ApJ*, 321, 305
- Davis, S. W., Woo, J.-H., & Blaes, O. M. 2007, *ApJ*, 668, 682
- Du, P., Lu, K.-X., Zhang, Z.-X., et al. 2016, *ApJ*, 825, 126
- Du, R., Ho, L. C., Ding, Y., & Li, R. 2024, *arXiv e-prints*, arXiv:2412.09451
- Ferland, G. J., Done, C., Jin, C., Landt, H., & Ward, M. J. 2020, *MNRAS*, 494, 5917
- Gaskell, C. M. 2009, *NewAR*, 53, 140
- GRAVITY Collaboration, Amorim, A., Bourdarot, G., et al. 2024, *A&A*, 684, A167
- Haardt, F., & Maraschi, L. 1991, *ApJL*, 380, L51
- Hall, P. B., Sarrouh, G. T., & Horne, K. 2018, *ApJ*, 854, 93
- Harikane, Y., Zhang, Y., Nakajima, K., et al. 2023, *ApJ*, 959, 39
- Huang, J., Jiang, Y.-F., Feng, H., et al. 2023, *ApJ*, 945, 57
- Hutsemékers, D., Sluse, D., Savić, D. V., & Richards, G. T. 2023, *A&A*, 672, A45
- Jiang, Y.-F., Blaes, O., Stone, J. M., & Davis, S. W. 2019a, *ApJ*, 885, 144
- Jiang, Y.-F., Stone, J. M., & Davis, S. W. 2014, *ApJ*, 796, 106
- . 2019b, *ApJ*, 880, 67
- Juodžbalis, I., Maiolino, R., Baker, W. M., et al. 2024, *arXiv e-prints*, arXiv:2403.03872
- King, A. 2024, *MNRAS*, 531, 550
- Kocevski, D. D., Onoue, M., Inayoshi, K., et al. 2023, *ApJL*, 954, L4
- Kubota, A., & Done, C. 2019, *MNRAS*, 489, 524
- Lambrides, E., Garofali, K., Larson, R., et al. 2024, *arXiv e-prints*, arXiv:2409.13047
- Lasota, J. P., Vieira, R. S. S., Sadowski, A., Narayan, R., & Abramowicz, M. A. 2016, *A&A*, 587, A13
- Lupi, A., Haardt, F., Dotti, M., et al. 2016, *MNRAS*, 456, 2993
- Lupi, A., Trinca, A., Volonteri, M., Dotti, M., & Mazzucchelli, C. 2024, *A&A*, 689, A128
- Madau, P. 1988, *ApJ*, 327, 116
- Madau, P., & Haardt, F. 2024, *ApJL*, 976, L24
- Madau, P., Haardt, F., & Dotti, M. 2014, *ApJL*, 784, L38
- Maiolino, R., Scholtz, J., Curtis-Lake, E., et al. 2024a, *A&A*, 691, A145
- Maiolino, R., Risaliti, G., Signorini, M., et al. 2024b, *arXiv e-prints*, arXiv:2405.00504
- Marin, F. 2014, *MNRAS*, 441, 551
- McKinney, J. C., Tchekhovskoy, A., Sadowski, A., & Narayan, R. 2014, *MNRAS*, 441, 3177
- Meier, D. L. 2012, *Black Hole Astrophysics: The Engine Paradigm*, doi:10.1007/978-3-642-01936-4
- Narayan, R., Nityananda, R., & Wiita, P. J. 1983, *MNRAS*, 205, 1103
- Netzer, H. 2019, *MNRAS*, 488, 5185
- Ogawa, T., Mineshige, S., Kawashima, T., Ohsuga, K., & Hashizume, K. 2017, *PASJ*, 69, 33
- Pacucci, F., & Narayan, R. 2024, *ApJ*, 976, 96
- Paczynsky, B., & Wiita, P. J. 1980, *A&A*, 88, 23
- Panda, S. 2021, *A&A*, 650, A154
- Pezzulli, E., Valiante, R., & Schneider, R. 2016, *MNRAS*, 458, 3047
- Pognan, Q., Trakhtenbrot, B., Sbarrato, T., Schawinski, K., & Bertemes, C. 2020, *MNRAS*, 492, 4058
- Pozo Nuñez, F., Haas, M., Ramolla, M., et al. 2014, *A&A*, 568, A36
- Rybicki, G. B., & Lightman, A. P. 1986, *Radiative Processes in Astrophysics*
- Sadowski, A. 2009, *ApJS*, 183, 171
- Sadowski, A., Narayan, R., Tchekhovskoy, A., et al. 2015, *MNRAS*, 447, 49
- Savić, D. V., Hutsemékers, D., & Sluse, D. 2024, *A&A*, 687, A114

- Sikora, M. 1981, *MNRAS*, 196, 257
- Sikora, M., & Wilson, D. B. 1981, *MNRAS*, 197, 529
- Tang, J.-J., Goto, T., Ohshima, Y., et al. 2019, *MNRAS*, 484, 2575
- Tozzi, G., Maiolino, R., Cresci, G., et al. 2023, *MNRAS*, 521, 1264
- Übler, H., Maiolino, R., Curtis-Lake, E., et al. 2023, *A&A*, 677, A145
- Veledina, A., Muleri, F., Poutanen, J., et al. 2024, *Nature Astronomy*, 8, 1031
- Volonteri, M., Silk, J., & Dubus, G. 2015, *ApJ*, 804, 148
- Wang, J.-M., Qiu, J., Du, P., & Ho, L. C. 2014, *ApJ*, 797, 65
- Wielgus, M., Yan, W., Lasota, J. P., & Abramowicz, M. A. 2016, *A&A*, 587, A38
- Wiita, P. J. 1982, *ApJ*, 256, 666
- Yue, M., Eilers, A.-C., Ananna, T. T., et al. 2024, *ApJL*, 974, L26
- Zeltyn, G., & Trakhtenbrot, B. 2022, *ApJ*, 929, 21